Organic Semiconductors Hot Paper

How to cite: *Angew. Chem. Int. Ed.* **2022,** *61,* e202116527
International Edition: doi.org/10.1002/anie.202116527
German Edition: doi.org/10.1002/ange.202116527

Fully Conjugated Tetraoxa[8]circulene-Based Porous Semiconducting Polymers

Patrick W. Fritz[+], Tianyang Chen[+], Timur Ashirov, Anh-Dao Nguyen, Mircea Dincă, and Ali Coskun**

Abstract: Tetraoxa[8]circulenes (TOCs) are a class of hetero[8]circulenes featuring a planar cyclooctatetraene core with a mixed aromatic/antiaromatic motif that governs their electronic properties. Polymeric TOCs (pTOCs) have been the subject of several computational simulations because they are predicted to be low-band-gap semiconductors, but they have not been available synthetically yet. Here, we report the first example of pTOCs, a new family of porous semiconductors, synthesized under ionothermal conditions through the intermolecular cyclization of 1,4,5,8-anthracene tetrone. pTOCs are porous, with surface areas up to 1656 $m^2 g^{-1}$, and exhibit light-switchable and tunable semiconducting properties.

Introduction

Porous organic polymers (POPs) and covalent organic frameworks (COFs) have attracted considerable interest due to their permanent porosity, chemical and structural tunability, and the potential for charge transport. Although COFs are often perceived to have an inherent advantage over POPs in terms of electrical conductivity due to their crystallinity, many COFs involve polarized linkages,[1] such as B–O and C=N, which naturally leads to decreased conjugation both energetically and spatially, and may hinder through-bond carrier migration.[2] POPs, on the other hand, are often obtained under kinetically controlled reaction conditions that involve a broad range of bond connections, including nonpolarized C–C and C=C bonds, thus facilitating the formation of semiconducting materials with low band gaps even when amorphous materials are formed.[3] A variety of strategies can be applied to tune the electronic structures, band gaps, and thus the charge transport properties of POPs. To this end, among many others,[3b,4] Coskun et al. have recently reported a facile strategy to tune the band gap of POPs based on an acid-catalyzed cyclization reaction.[5]

Hetero[8]circulenes have received substantial interest due to their optoelectronic properties, enabling their use as active materials in OLEDs[6] and OFETs.[7] One of the archetypal classes of hetero[8]circulenes, tetraoxa[8]-circulenes (TOCs), feature a planar structure and an antiaromatic cyclooctatetraene (COT) core,[8] resulting in unique electronic structures and redox switchable aromatic motifs.[9] The aromaticity of TOCs has been extensively studied both computationally[10] and experimentally[11] in molecular systems. Recently, a series of triptycene-bearing TOCs were reported and proposed as chemical sensors and as host materials for fullerenes.[12] Given its rigid molecular structure and extended conjugation, we envisioned TOC to be a promising building block for electrically conductive POPs featuring the intrinsic properties of TOCs as predicted by several computational studies.[13]

Herein, we report a polymerized version of TOC, pTOC. To our knowledge, this is the first example of a polymeric structure with this unique building block. The pTOC exhibits a two-dimensional (2D) extended ladder-type polymeric structure with three-dimensional (3D) characteristics. With a porosity of up to 1656 $m^2 g^{-1}$, pTOCs exhibit intrinsic electrical conductivity ranging from 1.0×10^{-6} $S cm^{-1}$ to 1.7×10^{-5} $S cm^{-1}$, which varies with the synthesis temperatures and can be further improved by doping.

Results and Discussion

Our initial attempts to obtain pTOCs mimicked the 1970 Högberg TOC synthesis based on the cyclization of 1,4-naphthoquinone[14] (Figure 1A). However, the treatment of 1,4,5,8-anthracenetetrone (AT)[15] with Lewis acids such as $AlCl_3$ and BF_3OEt_2 under solvothermal conditions did not yield any precipitate despite extensive screening of reaction temperatures, duration, or solvents (Table S1 and S2). Early research on TOCs suggested that dihydroxy species are formed as intermediates prior to dehydration and subsequent cyclization. Considering the likely poor solubility of the intermediates in our case, we surmised that the reaction

[*] P. W. Fritz,[+] T. Ashirov, A.-D. Nguyen, Prof. A. Coskun
Department of Chemistry, University of Fribourg,
Chemin du Musée 9, 1700 Fribourg (Switzerland)
E-mail: ali.coskun@unifr.ch

T. Chen,[+] Prof. M. Dincă
Department of Chemistry, Massachusetts Institute of Technology,
77 Massachusetts Ave, Cambridge, MA 02139 (USA)
E-mail: mdinca@mit.edu

[+] These authors contributed equally to this work.

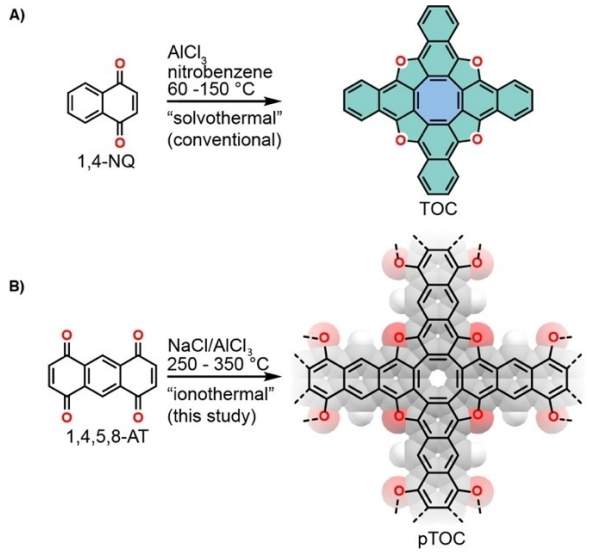

Figure 1. A) Cyclooligomerization of naphthoquinone under Lewis acidic conditions. The aromatic part of the molecule is highlighted in green and the antiaromatic COT-core in blue. B) Polymerization of 1,4,5,8-anthracene tetrone (AT) under ionothermal conditions. The structure of pTOC is shown along with its model structure as an overlay.

temperature was not high enough to facilitate cyclization. To enable more facile dehydration and hence induce condensation, we thus moved from a solvothermal approach to an ionothermal approach. Indeed, heating AT in a eutectic mixture of $AlCl_3$/NaCl[16] at temperatures ranging from 250 to 350 °C produced black solids, named pTOC-*temp*, where *temp* represents the reaction temperature, in 80–90 % yield (Figure 1B). The temperature range was specifically chosen to avoid carbonization, which is commonly reported to take place above 400 °C under ionothermal conditions.[17]

Solid-state (SS) cross-polarization magic-angle spinning (CP-MAS) ^{13}C NMR analysis of TOC and pTOC-350 confirmed the formation of pTOCs (Figure 2A). The ^{13}C NMR spectrum of TOC shows two peaks at 149 ppm (C atoms attached to the O) and 112 ppm (C atoms of the COT core), whereas the bulk of aromatic C atoms are located at 127, 123, and 120 ppm. In contrast, the ^{13}C spectrum of pTOC-350 shows broader features, implying the formation of an extended structure. Although the peaks shift slightly to a lower field upon polymerization, the peak positions are still in agreement with the TOC. The broad features in the pTOC-350 spectrum are also expected given its amorphous nature (Figure S5). Electron paramagnetic resonance (EPR) of pTOC-350 confirms the presence of organic radicals with an isotropic signal at $g = 2.007$ (Figure S12). These radicals are likely localized on defects such as unreacted/terminal carbonyl moieties and contribute to the electron conduction given that the EPR signal has Lorentzian line broadening.[18] Indeed, the ^{13}C SS NMR spectrum of pTOCs also shows a peak at 182 ppm, indicative of residual/terminal carbonyl moieties (Figure S1).

Fourier-transform infrared (FT-IR) spectroscopy, recorded in transmission mode with KBr pellets and in ATR mode (Figure S2A–C), revealed the expected C–O stretching bands at 660 and 850 cm^{-1}, and confirmed residual carbonyl bands at 1660 cm^{-1}.[19] Additional bands at 3050 and 1600 cm^{-1} correspond to C–H and C=C stretching modes, respectively. Absorbed water molecules in pTOCs result in very broad bands spanning the ≈1800 cm^{-1}–4000 cm^{-1} range, which are diminished in the spectra recorded by diffuse reflectance infrared Fourier-transform spectroscopy (DRIFTS) under N_2 (Figure S3). DRIFTS also shows that the intensity of the residual carbonyl vibrational bands between 1800 cm^{-1} and 1650 cm^{-1} decreases with higher reaction temperature, consistent with a higher degree of polymerization.

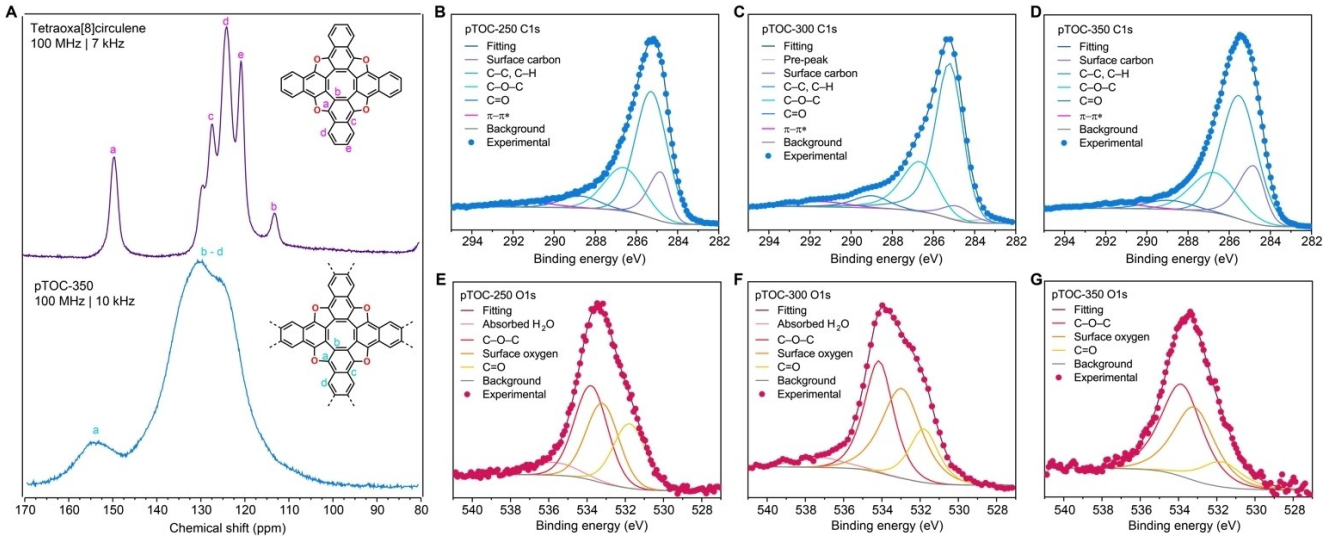

Figure 2. Spectroscopic characterization of pTOCs. A) Solid-state CP-MAS ^{13}C NMR spectra of tetraoxa[8]circulene (purple) and pTOC-350 (blue). B–D) C 1s XPS spectra and deconvolution of the pTOCs. E–G) O 1s XPS spectra and deconvolution of the pTOCs.

The composition of pTOCs was confirmed by X-ray photoelectron spectroscopy (XPS), which revealed that the C/O ratio varied with the reaction temperature (Figure S9, Table S3). Thus, pTOC-350 exhibits the highest C/O ratio of 7.48, close to the theoretical value of 7. This corresponds to the highest degree of polymerization among all pTOCs and is in agreement with the DRIFTS data. The slight deviation from the theoretical C/O value can be attributed to the cleavage of oxygen moieties at high reaction temperatures. With a C/O ratio of 6.89, pTOC-250 likely maintains extra oxygen atoms due to incomplete polymerization. The deconvolution of the C1s signal in high-resolution XPS spectra of pTOCs showed C–O–C components of the furane moieties at ≈286.7 eV that are consistent with literature values,[20] further verifying the in situ formation of tetraoxa-[8]circulene moieties (Figure 2B–D, Table S4–S10). The ratio of the C=O to C–O–C intensity decreases with increasing reaction temperature (Table S4–S6, S8) and is consistent with the higher degree of polymerization in pTOC-350. This result is further verified by the deconvolution of the O1s region, where the C=O component is almost negligible for pTOC-350 (Figure 2E–G, Table S7–S9), confirming that a higher reaction temperature is necessary to facilitate dehydration and subsequent aromatization of the polymer backbone (Figure 2B–G).

Raman spectra of the pTOCs were recorded using a Raman microscope at an excitation wavelength of 535 nm. The polymers showed two strong peaks at 1365 cm^{-1} and 1595 cm^{-1} (Figure S4) assigned as D (defect) and G (graphene) bands, respectively. This behavior has also been observed in fully conjugated systems prepared under solvothermal conditions.[3a,21] The I_D/I_G ratio decreases with increasing reaction temperature, from 0.75 for pTOC-250 to 0.62 for pTOC-350, indicating both the increased proportion of fused aromatic rings and decreased defects with increasing reaction temperature..[22] These compositional changes were also reflected macroscopically in the morphology of the various pTOCs. Thus, scanning electron microscopy (SEM) revealed that samples produced at elevated temperatures present as much smoother, more regular particles that contrast with the irregular, highly corrugated microparticles produced at lower temperatures (Figure S6).

The polymeric samples are consistent in their thermal behavior: pTOCs do not exhibit any mass loss below 450 °C (decomposition temperature, $T_d > 450$ °C) except for the initial removal of moisture absorbed from ambient air (Figure S7). By contrast, the AT precursor loses significant mass below 200 °C.

An idealized, defect-free structure of pTOC was modeled using Materials Studio assumed a square 2D lattice, which gave a π–π stacking distance of ≈3.4 Å (Figure S10). A Connolly surface analysis of this structure gave micropores with a diameter of approximately 5 Å (Figure S11). N_2 sorption isotherms (Figure 3A) at 77 K provided experimental evidence for permanent microporosity: all pTOCs exhibited type I isotherms with significant adsorption at low partial pressures below 0.11 P/P_0 (Figure S8A–F). A slight desorption hysteresis at higher relative pressures indicated the presence of mesopores, most likely due to the imperfect

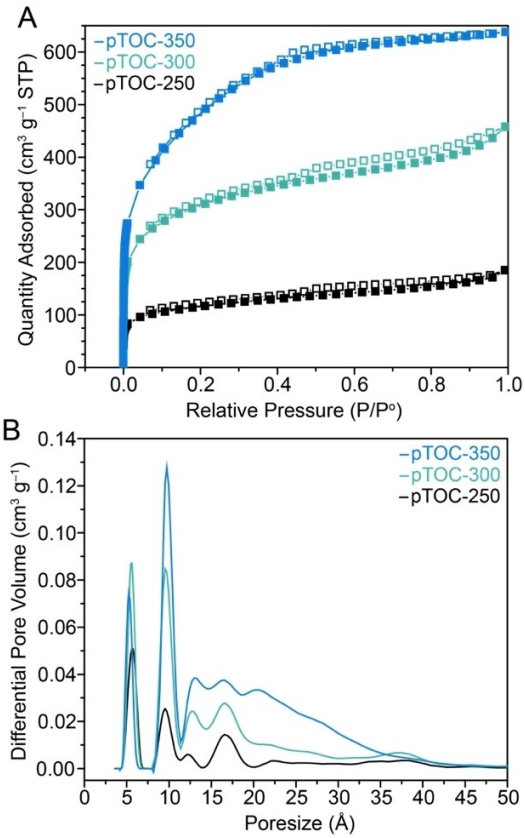

Figure 3. Gas sorption analysis of pTOCs: A) N_2 isotherms of pTOC-250 (black), pTOC-300 (green) and pTOC-350 (blue) at 77 K. Filled and empty symbols represent adsorption and desorption, respectively. B) NLDFT pore-size distribution of pTOC-250 (black), pTOC-300 (green) and pTOC-350 (blue).

stacking and the amorphous nature of the samples. Interestingly, the surface area, obtained by fitting the isotherms to the Brunauer–Emmett–Teller (BET) model, increased with the reaction temperature from 411 $m^2 g^{-1}$ to 1075 $m^2 g^{-1}$ and 1656 $m^2 g^{-1}$ for pTOC-250, pTOC-300, and pTOC-350, respectively (Table 1). Analysing the N_2 isotherm data with nonlocal density functional theory (NLDFT) (Figure 3B) confirmed non-uniform pore size distributions with peaks at 0.53 nm, 0.97 nm, and larger pores ranging from 1.3 nm to 4 nm. Remarkably, the smallest pore size obtained from NLDFT analysis is in good agreement with the value observed in the idealized structure. As such, we propose that the smallest pores originate from the stacked 2D layers with various sizes, and they interconnect to form an overall amorphous structure that gives rise to larger micropores and mesopores. This hypothesis is in line with the higher porosity for pTOC-350 and is further supported by the fact that the proportion of 0.5 nm relative to 0.9 nm pores increases with temperature.

A first hint for the degree of conjugation in pTOC comes from diffuse-reflectance UV/Vis (DRUV/Vis) spectroscopy. DRUV/Vis spectra of pTOC powders diluted in KBr show broad absorption that tails significantly into the near infrared (NIR) region, suggesting the formation of extended

structures (Figure 4A). The absence of sharp absorption edges is likely the result of the disordered structure of polymers. Interestingly, both pTOC-250 and pTOC-300 exhibit absorption maxima at around 500 nm with shoulders at 800 nm, substantially red-shifted relative to the absorption maximum of ≈350 nm for pTOC-350, despite their lower degree of polymerization. These differences likely stem from different interlayer interactions in the three samples. Plotted in Tauc coordinates, the DRUV/Vis spectra reveal optical band gaps (E_o) of 1.31 eV, 1.49 eV and 1.88 eV for pTOC-250, pTOC-300 and pTOC-350, respectively (Figure 4B). Notably, the band gaps of pTOC-250 and pTOC-300 are significantly smaller than the theoretical value for a single layer of pTOC (i.e., no inter-layer interaction), whereas that of pTOC-350 is quite similar.[13c] Encouraged by the broad optical absorption and relatively low E_o of pTOCs, two-probe electrical conductivity measurements of pressed pellets were performed (Table 2, Figure S13). Consistent with E_o progression, pTOC-250 and pTOC-300 showed higher average conductivities of 1.7×10^{-5} S cm^{-1} and 1.2×10^{-5} S cm^{-1}, respectively, whereas pTOC-350 had a maximal average conductivity of 3.3×10^{-6} S cm^{-1}, when the synthesis time was increased from 3 to 5 days (Figure S14). These results indicate that there is no correlation between the synthesis temperature and the conductivities of pTOCs. Four-probe devices of pTOC-350 exhibited a very similar conductivity value of 1.19×10^{-6} S cm^{-1}, indicating the negligible influence of contact resistance. Whereas most COFs are based on polarized linkages, a few examples of fully conjugated COFs through pyrazine, cyano-vinylene or vinylene linkages have also been reported recently.[23] Compared to these, pTOCs maintain a higher degree of sp^2 conjugation without strongly polarizing functionalities or building blocks and furthermore demonstrate the realization of electrical conductivity with highly tunable porosity (Table S13). In order to prove that the residual Cl$^-$ ions are not contributing to the conductivity of the pTOCs, we conducted conductivity measurements of pTOC-350 after doping with NaCl, which showed a slightly reduced conductivity of 1.8×10^{-7} S cm^{-1} (Figure S15).

Interestingly, the electrical conductivity of pTOCs revealed negative photo-response, decreasing by more than one order of magnitude after the four-probe device was exposed to light and low-intensity red laser (630–670 nm) (Figure 4C, S16). We note that although a photo-response is not unusual for organic electronic materials, the majority are positively photo-conductive, whereas negative photo-conductivity is much less common.[24] We attribute it to the

Table 2: Average room-temperature conductivities of pTOCs.

Materials	Conductivity [S cm^{-1}]
pTOC-250	1.7×10^{-5}
pTOC-300	1.2×10^{-5}
pTOC-350	1.0×10^{-6}
pTOC-350-LR	1.2×10^{-5}
pTOC-350-I_2 (RT doping)	5.0×10^{-6}
pTOC-350- I_2 (50 °C doping)	4.1×10^{-4}
pTOC-350-I_2 (vacuum 3 days)	1.6×10^{-5}

Table 1: N_2 sorption data for pTOCs at 77 K.

Sample	BET[a] [m^2 g^{-1}]	S_{micro}[b] [m^2 g^{-1}]	S_{ext}[c] [m^2 g^{-1}]	V_{total}[d] [cm^3 g^{-1}]	V_{micro}[e] [cm^3 g^{-1}]	V_{ext}[f] [cm^3 g^{-1}]	Ratio of 0.5/0.9 nm pores[g]
pTOC-250	411	200	211	0.286	0.086	0.200	1.50
pTOC-300	1075	481	594	0.710	0.215	0.495	0.66
pTOC-350	1656	530	1126	0.989	0.245	0.664	0.36

[a] BET surface areas calculated over the pressure range (P/P_0) of 0.01–0.11. [b] Micropore surface area calculated using the *t*-plot method. [c] $S_{ext}=S_{total}-S_{micro}$. [d] Total pore volume obtained at $P/P_0=0.99$. [e] Micropore volume calculated using the *t*-plot method. [f] $V_{ext}=V_{total}-V_{micro}$. [g] Ratio of 0.5/0.9 nm pores calculated from the integral of the pore-size distribution (PSD) plots.

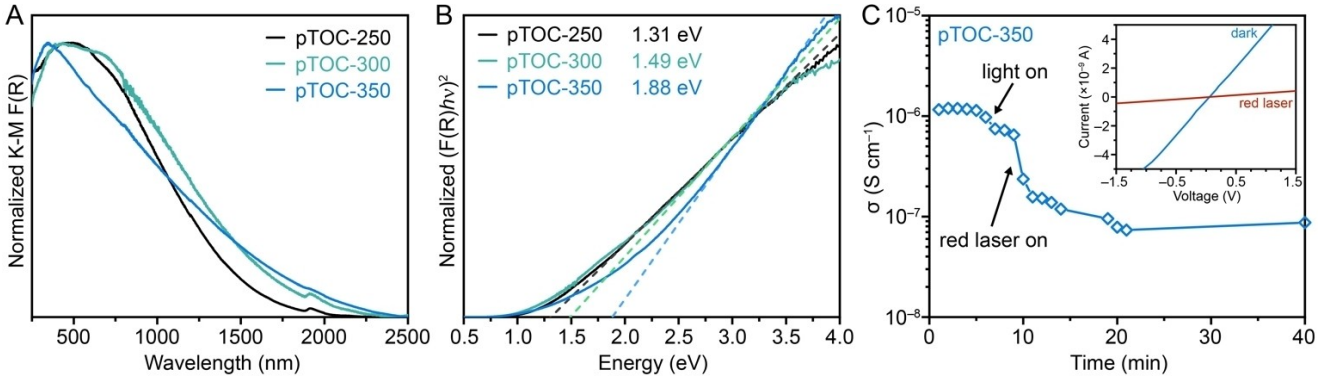

Figure 4. Spectroscopic analysis of pTOCs: A) DRUV spectra of pTOC-250 (black), pTOC-300 (green), and pTOC-350 (blue) diluted in KBr, respectively. B) Tauc plots of the DRUV spectra. C) The evolution of electrical conductivity of pTOC-350 when exposed to light and red laser (< 5 mW).

light-induced generation of shallow trap states that impedes the transport of charge carriers.[25] To verify the stability of pTOCs under photo-irradiation, we conducted long-term exposure experiments followed by characterization via HR-XPS (Figure S17 and Table S11–S12) and DRUV/Vis (Figure S18) spectroscopy, the results of which indicate that the chemical structure of pTOC remains unchanged. With well-defined residual carbonyl defects present, post-synthetic modification (PSM) of these sites allows the tuning of electronic properties of pTOCs. We conducted PSM of residual carbonyls in pTOC-350 using Lawesson's reagent (LR) (Figure 5A). This treatment transforms C=O groups to C=S groups, as confirmed by the reduced intensity of residual C=O and the appearance of C=S vibrational bands in DRIFTS (Figure S22), and the presence of sulfur, as revealed by XPS analysis (Figure S20, S21). Treatment with the LR increases the conductivity of pTOC-350 by nearly one order of magnitude to 1.2×10^{-5} S cm^{-1} (Table 2).

pTOCs also provide a promising platform for bulk doping given their high porosity and high heteroatom content. The bulk doping of pTOC-350 was realized upon exposure to I_2 vapor at room temperature and the incorporation of iodine again confirmed by XPS (Figure S23). Two different iodine-containing species were found at binding energies of 619.1 eV and 620.6 eV ($3d_{5/2}$ transition of iodine), which are assigned to reduced species and trapped I_2, respectively. pTOC-350-I_2 showed a slight increase of conductivity to 5.0×10^{-6} S cm^{-1} (Figure S24). Notably, the conductivity of pTOC-350 enhanced substantially to 4.1×10^{-4} S cm^{-1} after exposure to I_2 at 50 °C, a value that is in line with some of the most conductive POPs.[2] DRIFTS of pTOC-350-I_2 revealed negligible changes except for the appearance of intense Drude-type background absorption (Figure S25), suggesting a significant increase in free carrier concentration upon I_2 doping.

Variable-temperature (VT) conductivity measurements (Figure S26–S27) revealed semiconducting behavior for pTOC-350 and pTOC-350-I_2 between 375 K and 100 K (Figure 5B). Fitting the data of pTOC-350 to the Arrhenius equation for conventional thermally activated hopping transport between the nearest-neighbor localized states, $\sigma = \sigma_0\exp(-E_a/k_BT)$, where σ is the electrical conductivity, σ_0 is a material-based prefactor, k_B is the Boltzmann constant, and T is the absolute temperature, yielded the activation energy for hopping, $E_a = 0.195$ eV. This value is lower than that of a 3D fully sp^2-hybridized graphitic polymer (3D-p-POP) we reported previously.[3a] However, the variable temperature conductivity data for pTOC-350-I_2 deviates significantly from linear behavior when modeled by thermally activated hopping (Figures S28). Instead, the data fits better to the variable-range hopping (VRH) model, $\sigma = \sigma_0\exp[-(T_0/T)^{1/4}]$, where σ_0 is the conductivity at infinite temperature, and T_0 is the Mott temperature.[26] The better fit to the VRH model suggests that in the I_2-doped sample, more delocalized electronic states and/or better overlap of charge carrier wavefunctions dominate transport.[27]

To understand the change in the electronic structures of pTOCs upon post-synthetic modification and doping, we conducted DRUV/Vis and valence-band XPS (VB-XPS). pTOC-350-LR and pTOC-350-I_2 both exhibit red-shifted absorption (Figure 5C) and a decrease in E_o from 1.88 eV to 1.63 eV, and 1.55 eV, respectively, accompanied by an increase in the background absorption and the appearance of a broad NIR band owing to the polaronic transitions and/or interlayer interactions (Figure S29). The absorption maximum of pTOC-350-I_2 red-shifted to ≈436 nm, as might be expected for significantly delocalized electronic states revealed by VT conductivity measurements. The main absorption band for pTOC-350-LR showed no change, highlighting the different outcomes between bulk doping and post-synthetic modification. VB-XPS, which reports on the density of states (DOS) near the Fermi level E_F, revealed a significant increase of DOS for pTOC-350-I_2, further substantiating the increase in carrier concentration (Figure 5D, S30) upon I_2 doping, contrasting with the minimal changes observed for the LR-treated sample.

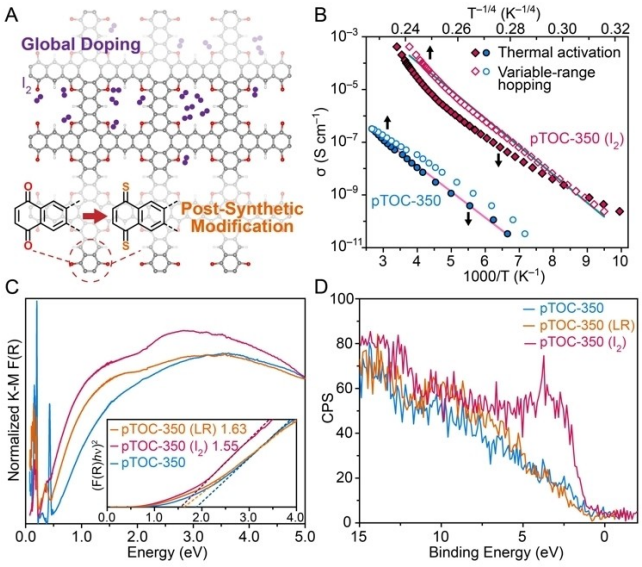

Figure 5. Doping and post-synthetic modification: A) Schematic representations of PSM and bulk doping. B) Variable-temperature electrical conductivity measurements of pTOC-350 and pTOC-350-I_2. Solid and hollow symbols represent data plotted for the thermal hopping model and the VRH model, respectively. Solid lines are the best fits. C) Diffuse reflectance UV/Vis-NIR and DRIFTS spectra of pTOC-350 (blue), pTOC-350-LR (orange), and pTOC-350-I_2 (red). D) VB-XPS of the samples shown in (C).

Conclusion

In summary, we have introduced a new class of semiconducting two-dimensional porous organic polymers featuring tetraoxa[8]circulene building blocks, which—to date—were only envisioned in theoretical simulations. The polymers, obtained via ionothermal synthesis, feature high porosity, semiconductor behavior, and unusual negative photoconductivity. The conductivity of the pTOCs can be tuned through both post-synthetic modification and bulk doping, where both their carrier concentration and elec-

tronic band structures are readily controlled. Altogether, these results highlight the potential of pTOCs as a new family of porous semiconductors.

Acknowledgements

A.C. thanks the Swiss National Science Foundation (SNSF) for funding of this research (200021-188572). Work in the Dinca lab was supported by the National Science Foundation (Waterman Award to MD; DMR-1645232). We are grateful to Prof. Stefan Salentinig and Rafael V. de Melo Freire for access and help with the Raman measurements. Open access funding provided by Universite de Fribourg.

Conflict of Interest

The authors declare no conflict of interest.

Data Availability Statement

The data that support the findings of this study are available from the corresponding author upon reasonable request.

Keywords: Doping · Porous Organic Polymers · Post-Synthetic Modification · Semiconductors · Tetraoxa[8]Circulenes

[1] T. Joshi, C. Chen, H. Li, C. S. Diercks, G. Wang, P. J. Waller, H. Li, J.-L. Bredas, O. M. Yaghi, M. F. Crommie, *Adv. Mater.* **2019**, *31*, 1805941.
[2] P. W. Fritz, A. Coskun, *Chem. Eur. J.* **2021**, *27*, 7489–7501.
[3] a) Y. Byun, L. S. Xie, P. Fritz, T. Ashirov, M. Dincă, A. Coskun, *Angew. Chem. Int. Ed.* **2020**, *59*, 15166–15170; *Angew. Chem.* **2020**, *132*, 15278–15282; b) Y. S. Kochergin, D. Schwarz, A. Acharjya, A. Ichangi, R. Kulkarni, P. Eliášová, J. Vacek, J. Schmidt, A. Thomas, M. J. Bojdys, *Angew. Chem. Int. Ed.* **2018**, *57*, 14188–14192; *Angew. Chem.* **2018**, *130*, 14384–14388.
[4] a) Y. S. Kochergin, Y. Noda, R. Kulkarni, K. Škodáková, J. Tarábek, J. Schmidt, M. J. Bojdys, *Macromolecules* **2019**, *52*, 7696–7703; b) B. Bonillo, R. S. Sprick, A. I. Cooper, *Chem. Mater.* **2016**, *28*, 3469–3480.
[5] J. Lee, O. Buyukcakir, T.-w. Kwon, A. Coskun, *J. Am. Chem. Soc.* **2018**, *140*, 10937–10940.
[6] a) K. B. Ivaniuk, G. V. Baryshnikov, P. Y. Stakhira, S. K. Pedersen, M. Pittelkow, A. Lazauskas, D. Volyniuk, J. V. Grazulevicius, B. F. Minaev, H. Ågren, *J. Mater. Chem. C* **2017**, *5*, 4123–4128; b) R. R. Valiev, R. M. Gadirov, K. M. Degtyarenko, D. V. Grigoryev, R. T. Nasubullin, G. V. Baryshnikov, B. F. Minaev, S. K. Pedersen, M. Pittelkow, *Chem. Phys. Lett.* **2019**, *732*, 136667.
[7] A. Dadvand, F. Cicoira, K. Y. Chernichenko, E. S. Balenkova, R. M. Osuna, F. Rosei, V. G. Nenajdenko, D. F. Perepichka, *Chem. Commun.* **2008**, 5354–5356.
[8] F. Fouad, S. D. Bunge, B. D. Ellman, R. J. Twieg, *Acta Crystallogr. Sect. C* **2012**, *68*, o465–o467.
[9] F. Chen, Y. S. Hong, S. Shimizu, D. Kim, T. Tanaka, A. Osuka, *Angew. Chem. Int. Ed.* **2015**, *54*, 10639–10642; *Angew. Chem.* **2015**, *127*, 10785–10788.
[10] a) C. B. Nielsen, T. Brock-Nannestad, P. Hammershoj, T. K. Reenberg, M. Schau-Magnussen, D. Trpcevski, T. Hensel, R. Salcedo, G. V. Baryshnikov, B. F. Minaev, M. Pittelkow, *Chem. Eur. J.* **2013**, *19*, 3898–3904; b) G. V. Baryshnikov, R. R. Valiev, N. N. Karaush, D. Sundholm, B. F. Minaev, *Phys. Chem. Chem. Phys.* **2016**, *18*, 8980–8992; c) G. V. Baryshnikov, R. R. Valiev, N. N. Karaush, V. A. Minaeva, A. N. Sinelnikov, S. K. Pedersen, M. Pittelkow, B. F. Minaev, H. Agren, *Phys. Chem. Chem. Phys.* **2016**, *18*, 28040–28051; d) S. Radenković, I. Gutman, P. Bultinck, *J. Phys. Chem. A* **2012**, *116*, 9421–9430.
[11] M. Pittelkow, T. Hensel, N. Andersen, M. Plesner, *Synlett* **2016**, *27*, 498–525.
[12] N. G. Petrov, P. Chartier, T. Maris, J. D. Wuest, *J. Am. Chem. Soc.* **2022**, *144*, 556–572.
[13] a) G. V. Baryshnikov, B. F. Minaev, N. N. Karaush, V. A. Minaeva, *RSC Adv.* **2014**, *4*, 25843–25851; b) G. V. Baryshnikov, B. F. Minaev, N. N. Karaush, V. A. Minaeva, *Phys. Chem. Chem. Phys.* **2014**, *16*, 6555–6559; c) A. V. Kuklin, G. V. Baryshnikov, B. F. Minaev, N. Ignatova, H. Ågren, *J. Phys. Chem. C* **2018**, *122*, 22216–22222; d) L. V. Begunovich, A. V. Kuklin, G. V. Baryshnikov, R. R. Valiev, H. Ågren, *Nanoscale* **2021**, *13*, 4799–4811.
[14] H. Erdtman, H. E. Högberg, *Tetrahedron Lett.* **1970**, *11*, 3389–3392.
[15] F. Glöcklhofer, B. Stöger, J. Fröhlich, *Synth. Commun.* **2018**, *48*, 2358–2365.
[16] a) E. M. Levin, J. F. Kinney, R. D. Wells, J. T. Benedict, *J. Res. Natl. Bur. Stand. Sect. A* **1974**, *78*, 505–507; b) R. W. Berg, H. A. Hjuler, N. J. Bjerrum, *Inorg. Chem.* **1984**, *23*, 557–565.
[17] a) M. Liu, L. Guo, S. Jin, B. Tan, *J. Mater. Chem. A* **2019**, *7*, 5153–5172; b) K. Schwinghammer, S. Hug, M. B. Mesch, J. Senker, B. V. Lotsch, *Energy Environ. Sci.* **2015**, *8*, 3345–3353.
[18] K. Tadyszak, A. Musiał, A. Ostrowski, J. K. Wychowaniec, *Nanomaterials* **2020**, *10*, 798.
[19] J. Spanget-Larsen, D. Liang, E. Chen, E. Thulstrup, *Asian Chem. Lett.* **2000**, *4*, 121–134.
[20] G. Beamson, D. R. Briggs, *J. Chem. Educ.* **1993**, *70*, A25.
[21] S. Zheng, D. Shi, D. Yan, Q. Wang, T. Sun, T. Ma, L. Li, D. He, Z. Tao, J. Chen, *Angew. Chem. Int. Ed.* **2022**, *61*, e202117511; *Angew. Chem.* **2022**, *134*, e202117511.
[22] a) I. Childres, L. Jauregui, W. Park, H. Caoa, Y. P. Chena, *New Developments in Photon and Materials Research*, Nova, New York, **2013**, pp. 403–418; b) Y. Wang, D. C. Alsmeyer, R. L. McCreery, *Chem. Mater.* **1990**, *2*, 557–563.
[23] a) S. Wang, X.-X. Li, L. Da, Y. Wang, Z. Xiang, W. Wang, Y.-B. Zhang, D. Cao, *J. Am. Chem. Soc.* **2021**, *143*, 15562–15566; b) S. Wang, L. Da, J. Hao, J. Li, M. Wang, Y. Huang, Z. Li, Z. Liu, D. Cao, *Angew. Chem. Int. Ed.* **2021**, *60*, 9321–9325; *Angew. Chem.* **2021**, *133*, 9407–9411; c) M. Wang, M. Wang, H.-H. Lin, M. Ballabio, H. Zhong, M. Bonn, S. Zhou, T. Heine, E. Cánovas, R. Dong, X. Feng, *J. Am. Chem. Soc.* **2020**, *142*, 21622–21627; d) M. Wang, M. Ballabio, M. Wang, H.-H. Lin, B. P. Biswal, X. Han, S. Paasch, E. Brunner, P. Liu, M. Chen, M. Bonn, T. Heine, S. Zhou, E. Cánovas, R. Dong, X. Feng, *J. Am. Chem. Soc.* **2019**, *141*, 16810–16816.
[24] K. Y. Law, *Chem. Rev.* **1993**, *93*, 449–486.
[25] a) A. S. Chaves, H. Chacham, *Appl. Phys. Lett.* **1995**, *66*, 727–729; b) M. A. C. Fox, D. A., *Adv. Mater.* **1991**, 381–385.
[26] N. F. D. Mott, A. Edward, *Electronic Processes in Non-Crystalline Materials*, Oxford University Press, Oxford, **1979**.
[27] H. Tanaka, M. Hirate, S. Watanabe, S.-i. Kuroda, *Adv. Mater.* **2014**, *26*, 2376–2383.

Manuscript received: December 3, 2021
Accepted manuscript online: February 16, 2022
Version of record online: February 28, 2022